CORA Cork Open Research Archive
Cartlann Taighde Oscailte Chorcaí

Title	Pedestrian-to-vehicle communications in an urban environment: channel measurements and modeling
Authors	Doone, M. G.;Cotton, S. L.;Matolak, D. W.;Oestges, C.;Heaney, S. F.;Scanlon, William G.
Publication date	2019-03-01
Original Citation	Doone, M.G., Cotton, S.L., Matolak, D.W., Oestges, C., Heaney, S.F. and Scanlon, W.G., 2019. Pedestrian-to-vehicle communications in an urban environment: Channel measurements and modeling. IEEE Transactions on Antennas and Propagation, 67(3), (14pp). DOI: 10.1109/TAP.2018.2885461
Type of publication	Article (peer-reviewed)
Link to publisher's version	http://ieeexplore.ieee.org/stamp/stamp.jsp?tp=&arnumber=8576610&isnumber=8660595 - 10.1109/TAP.2018.2885461
Rights	© Doone et al. This work is licensed under a Creative Commons Attribution 3.0 License - https://creativecommons.org/licenses/by/3.0/
Download date	2026-10-30 11:54:55
Item downloaded from	https://hdl.handle.net/10468/7881



UCC
University College Cork, Ireland
Coláiste na hOllscoile Corcaigh

Pedestrian-to-Vehicle Communications in an Urban Environment: Channel Measurements and Modeling

Michael G. Doone, *Member, IEEE*, Simon L. Cotton, *Senior Member, IEEE*, David W. Matolak, *Senior Member, IEEE*, Claude Oestges, *Fellow, IEEE*, Sean F. Heaney, and William G. Scanlon, *Senior Member, IEEE*

***Abstract*— As wireless connectivity becomes increasingly ubiquitous, a greater emphasis will be placed upon the seamless integration of dissimilar networking technologies. One such example of this will occur in urban environments, where wearable devices and vehicular networks will operate in close proximity to one another. Clearly, a natural extension to both types of network is their interconnectivity through vehicle-to-pedestrian (V2P) or equivalently pedestrian-to-vehicle (P2V) communications as part of a much greater vehicle-to-X (V2X)-based intelligent transportation system. To this end, we empirically investigate the P2V communications channel at 5.8 GHz for the case of a moving vehicle when a person positioned by the edge of a road was either stationary or walking parallel to the side of the highway. The measurements considered a chest-mounted transmitter and four receiver locations on the vehicle covering the front wing mirrors and two positions on the roof, which simultaneously recorded the received signal power. To characterize the propagation mechanisms which are responsible for shaping the received signal in the P2V channel, we decomposed it into its path loss (PL), large-scale, and small-scale fading components. We first show that although there was evidence of interference caused by multiple rays interacting with one another, the popular two-ray ground-reflection PL model was unable to adequately describe the compounded effects of the vehicle and pedestrian's body on the signal attenuation in the majority of the considered scenarios. Instead, we found that the overall PL was well characterized using a dual-slope log-distance model, with lognormal large-scale fading. Due to the often severe small-scale fading that was observed in the P2V channel, we have been able to utilize the κ-μ extreme distribution with considerable success to characterize the worse than Rayleigh fading conditions which were encountered.**

***Index Terms*— κ-μ distribution, κ-μ extreme distribution, channel measurements, fading channels, path loss (PL), two-ray ground-reflection, vehicular communications, wearable communications.**

I. Introduction

RECENT years have seen the widespread uptake of wireless-enabled devices designed to be carried or worn by people [1], [2]. These devices, which are now commonly referred to as "wearables," have the potential to transform how society interacts, by forming vast people-driven networks that are not only capable of sharing information between themselves but also relaying data meant for other people and networks. Similarly, the adoption of wireless devices designed for the automotive market [3] has also been prevalent. Here, it is envisioned that vehicles will gather information on road traffic conditions, and through sharing of this information with nearby wireless devices, assist in improving road safety and help alleviate traffic congestion [4]. This unified infrastructure is often referred to as an intelligent transportation system (ITS) which, among other functions, will be critical for relaying time-sensitive safety information [5].

ITSs were originally conceived to include both Vehicle-to-Infrastructure (V2I) and Vehicle-to-Vehicle (V2V) communications, which enable the exchange of information between vehicles in the immediate vicinity, or provision information ahead of time to drivers who may be traveling through the area in the near future. The transmission of information between a moving vehicle and fixed infrastructure has been the subject of research for many years [6], [7], while communications between vehicles have only relatively recently been gaining momentum [8]–[10]. This has been popularized by the introduction of wireless access for vehicular environments [11], which defines enhancements to the IEEE 802.11 standard, enabling the architectures, and services required to allow wireless devices to communicate over the dedicated short-range communications (DSRC) frequency band [10]. In 1999, the U.S. federal communications commissions allocated 75 MHz of spectrum within the 5.9 GHz band for the use of ITSs. Similarly, in 2008, the European Telecommunications Standards Institute allocated 30 MHz of the spectrum also within the 5.9 GHz band, enabling the standardization of previously disparate systems.

Manuscript received March 13, 2018; revised October 5, 2018; accepted November 16, 2018. Date of publication December 14, 2018; date of current version March 5, 2019. This work was supported by the U.K. Engineering and Physical Sciences Research Council under Grant EP/L026074/1. *(Corresponding author: Simon L. Cotton.)*

M. G. Doone and S. L. Cotton are with the Centre for Wireless Innovation, Institute of Electronics, Communications, and Information Technology, Queen's University Belfast, Belfast BT3 9DT, U.K. (e-mail: mdoone03@qub.ac.uk; simon.cotton@qub.ac.uk).

D. W. Matolak is with the Department of Electrical Engineering, University of South Carolina, Columbia, SC 29208 USA (e-mail: matolak@cec.sc.edu).

C. Oestges is with the Institute of Information and Communication Technologies, Electronics, and Applied Mathematics, Université Catholique de Louvain, 1348 Louvain-la-Neuve, Belgium (e-mail: claude.oestges@uclouvain.be).

S. F. Heaney is with Jaguar Land Rover Gaydon, Warwick CV35 0RR, U.K. (e-mail: sheaney@jaguarlandrover.com).

W. G. Scanlon is with the Tyndall National Institute, University College Cork, Cork, T12 R5CP Ireland (e-mail: william.scanlon@tyndall.ie).

Color versions of one or more of the figures in this paper are available online at http://ieeexplore.ieee.org.

Digital Object Identifier 10.1109/TAP.2018.2885461

This work is licensed under a Creative Commons Attribution 3.0 License. For more information, see http://creativecommons.org/licenses/by/3.0/

As ITSs continue to evolve, it is envisaged that wearable and vehicular networks will eventually interoperate through so-called "vehicle-to-X" (V2X) or more precisely vehicle-to-pedestrian (V2P) communications. This will bring many benefits to users of both types of network. For example, through pedestrian-to-vehicle (P2V) communications, drivers will have an early warning on the numbers of pedestrians inhabiting in the local environment. In addition, both types of wireless node (wearable and vehicular) may act as relay nodes for one another and in the process provide multihop access to wireless networks outside their communicating range [12].

The propagation conditions encountered by both wearable and vehicular communications are known to be particularly challenging. For example, wearable devices can operate in a range of different environments (e.g., indoors, outdoors, in-vehicle, etc.), are subject to complex antenna-body electromagnetic interaction effects [13] and due to the low elevation of at least one end of the link, subject to frequent shadowing events caused by the wearer's body and the bodies of other persons in the local surroundings [14], [15]. In [14], it was found that the received signal power in a wearable device to base station link operating indoors at 2.4 GHz can deteriorate by as much as 50 dB due to human body shadowing, whereas for wearable-to-wearable applications operating in a low multipath environment such as outdoors, this effect may result in the communications link being lost entirely [15].

In a similar manner to wearable communications, vehicular communications can take place within diverse environments ranging from rural areas, highways, and interstates, through to densely and sparsely populated urban zones. Furthermore, these often occur at high velocities and in the presence of other moving vehicles, which can result in significant scattering and obstruction of the link [16]–[19]. Like antennas operating in close proximity to the human body, within vehicular communications, the antenna-vehicle interaction effects can have a considerable impact on the performance of communications [20]–[22]. Typically, antennas are mounted on the highest point of the vehicle (i.e., the roof) to reduce the interaction with the vehicle and surrounding low-lying objects, thus providing the best opportunity for unobstructed omnidirectional radiation in the horizontal plane. Nonetheless, in this case, the metallic structure of the roof acts as a ground plane which can reflect electromagnetic energy from the antenna above the horizontal plane, therefore reducing gain in the desired elevation for V2V channels [20]. Mecklenbrauker *et al.* [4] reported a drop in antenna directivity by as much as 6.5 dB in the horizontal plane as a direct result of the roof tapering. In modern vehicles, the roof may contain nonmetallic elements such as a sunroof, nonuniform surfaces, or railings mounted along the sides, which can further influence the antenna's radiation pattern [20], [23]. This was also reported in [21], [22], and [24], suggesting that the link quality for V2V communications depends significantly on the mounting location of the antenna. This has prompted investigations into alternative mounting locations, such as front and rear bumpers, wing mirrors, and even inside the vehicle [21]. Indeed, this observation motivates our investigation of alternate vehicular mounting points for the automobile side of the P2V communications scenarios studied here.

In the open literature, the few existing studies of communications between a pedestrian and a vehicle are largely based on understanding collision avoidance techniques, for the detection of so-called vulnerable road users [25]–[30]. Pedestrian detection within the automotive industry has been ongoing for many years, utilizing vision, laser, and radar techniques; however, these methods require an unobstructed optical view with the pedestrian, which is rarely the case in an urban environment. To extend the detection region to include hidden areas, methods based on wireless communications have also been investigated [25], [27]. David and Flach [25] investigated the channel latency of numerous wireless communications architectures, including Wi-Fi ad hoc networks and cellular communications, for sharing the position of pedestrians obtained by a global positioning system (GPS) enabled device with nearby vehicles. Hisaka and Kamijo [27] chose to detect the pedestrian's position based on localization utilizing dedicated Wi-Fi enabled receivers placed on the four corners of the vehicle. The analysis was limited to the detection of the pedestrian, and although significant variations in the received signal were observed, no statistical analysis of the channel dynamics was performed. It is worth noting that these investigations were all performed outside of the DSRC frequency band. This issue was addressed in [31] and [32], where a system was developed within the DSRC frequency band to provide information to both pedestrians and vehicles on nearby collision risks. In [33], the communications between the two mobile users were considered, one of which was located within a vehicle and another who was walking outside the vehicle. Although a statistical analysis of the mobile-to-mobile channel was undertaken, it was performed at 1.85 GHz, which is outside of the DSRC frequency band.

While previous measurements performed for channels involving people and separately channels involving vehicles have provided valuable insights, the differences in antenna type, height, mounting position, and the operating environment will result in fading conditions that are unlikely to accurately depict those experienced within the P2V channel. Previous work by Doone and Cotton [34]–[36] has presented some initial insights pertaining to the fading characteristics that occur within P2V communications channels. In [34], radio channel measurements were conducted at 5.8 GHz between a moving vehicle at different velocities and with a stationary pedestrian positioned by the side of the road. The experiments considered a transmitter (TX) mounted at different locations on the body and several receivers (RX) mounted on the vehicle. Though examples of the observed received signal power were presented, the analysis was limited to modeling only the small-scale fading using the Ricean distribution. Moreover, the previous work modeled the vehicle's journey in its entirety, without making a distinction between the line-of-sight (LOS) and non-LOS (NLOS) fading conditions, meaning it was not possible to quantify the effects of shadowing caused by both the vehicle and the pedestrian's body. This was later addressed in [36], by segmenting the data into

parts corresponding to when the vehicle "approached" and "receded" from the pedestrian, where fading conditions were observed to vary considerably as a result of the body-induced shadowing. This paper was also extended to complete the statistical analysis of the P2V channel by modeling the path loss and the large-scale fading components. It was found that by visually segmenting the data where the fading conditions appear to change considerably, the path loss (PL) was better modeled using a dual-slope model rather than the single-slope approach.

In this contribution, we further extend our work to include an improved small-scale fading analysis using the κ-μ extreme distribution. We also include a method for segmenting the channels by estimating the breakpoint distance that yields the optimal (in the least-squares sense) dual-slope PL model. Furthermore, by keeping the speed of the vehicle consistent and introducing scenarios where the pedestrian was walking, we have been able to examine how the movement of the pedestrian's body will further impact the P2V communications channel. Last, we investigate different antenna positions on the vehicle from those previously studied in [34]–[36] including the often omitted wing mirror positions, which, as will be demonstrated in the sequel, actually prove to be valuable and worth consideration for P2V communications.

The remainder of this paper is organized as follows. Section II outlines the measurement system, the experimental environment and the various scenarios investigated in this paper. Section III presents some initial observations on the channel measurements. Based on those observations, it then decomposes the channel and provides a characterization of the PL and large-scale fading that occurred, while in Section IV, the small-scale fading is characterized using the κ-μ extreme distribution. Finally, Section V completes this paper with some concluding remarks.

II. Measurement System, Environment, and Scenarios

A. Measurement System

The measurement system used in this paper consisted of five bespoke wireless nodes that operated at 5.8 GHz (chosen due to its close proximity to the 5.9 GHz DSRC band). All nodes were capable of operating as either a TX or RX, but for the purposes of this measurement campaign, one was configured as a TX and the remaining four as RX nodes, maintaining their mode of operation throughout. The nodes consisted of two parts: the RF section, which featured an ML5805 transceiver chip manufactured by RF Micro Devices, and a baseband controller section, which contained a dedicated PIC32MX microcontroller manufactured by Microchip Technology Incorporated. When acting as an RX, the baseband controller was programed to sample the received signal strength (RSS) from the ML5805 transceiver chip using a 10 bit analog-to-digital (ADC) converter. This was controlled using the onboard 32 bit timer interrupt, where a single RSS sample event was obtained by averaging 10 ADC readings to improve the signal-to-noise ratio of the system. All of the RX nodes were precalibrated using a Rohde & Schwarz SMU200A vector signal generator.

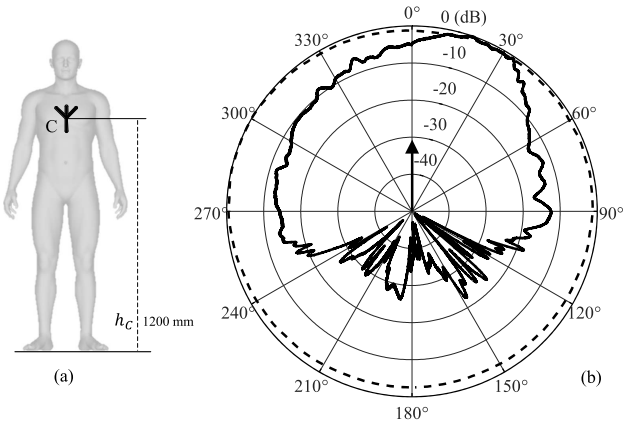


Fig. 1. (a) Illustration of the TX node position on the central chest (C) region of the pedestrian and (b) its measured azimuthal directivity pattern (black continuous line) with the same sleeve dipole antenna in free space (black dashed line). The upward arrow in (b) denotes the forward direction from the pedestrian's chest.

The RX nodes simultaneously logged the RSS samples at a rate of 10 kHz on a single laptop in real time, which was also equipped with a GPS receiver (G-STAR IV model BU-353S4) to record the position of the vehicle.

The node acting as the TX was precalibrated using a Rhode & Schwarz NRP-Z21 Power Meter and configured to transmit a continuous wave signal at 5.8 GHz with an output power of $+17.6$ dBm. A GPS receiver was also carried by the pedestrian so that their position could also be monitored throughout the field measurements. It should be noted that due to the vastly different sample rates between the wireless nodes and the GPS receivers (10 kHz vs. 1 Hz), a linear interpolation, postprocessing step was used to synchronize the RSS samples with the GPS data. This enabled the distance between the pedestrian and the vehicle to be computed using the Haversine formula. Approximately, seven million RSS samples were collected during the measurement campaigns presented in this paper. The RX noise threshold was determined prior to all experiments and the average was found to be -98.2 dBm. To ensure all channel data used in the analysis presented within this paper was above this noise threshold, the lowest recorded sample used for the purposes of modeling was -97.1 dBm.

The antenna type used by both the TX and the RX nodes was a $+2.3$ dBi sleeve dipole antenna (Mobile Mark model PSKN3-24/55S) connected directly to the RF front end of the radio using a SubMiniature version A connector. The TX antenna was mounted using Velcro in a vertically polarized orientation, parallel to the front central chest (C) region of an adult male of mass 75 kg and height 1.72 m, resulting in an antenna height of 1.2 m above the ground level as shown in Fig. 1(a). To maintain a consistent antenna-body separation distance throughout the experiments, a 5 mm dielectric spacer consisting of Rohacell HF 51 foam ($\epsilon_r = 1.07$) was placed between the antenna and the body surface. The vehicle chosen for this paper was a typical European, small three-door hatchback car with the dimensions as depicted in Fig. 2(a). Also, Fig. 2(a) shows the four antenna positions on the vehicle which were considered for this paper; these were the front

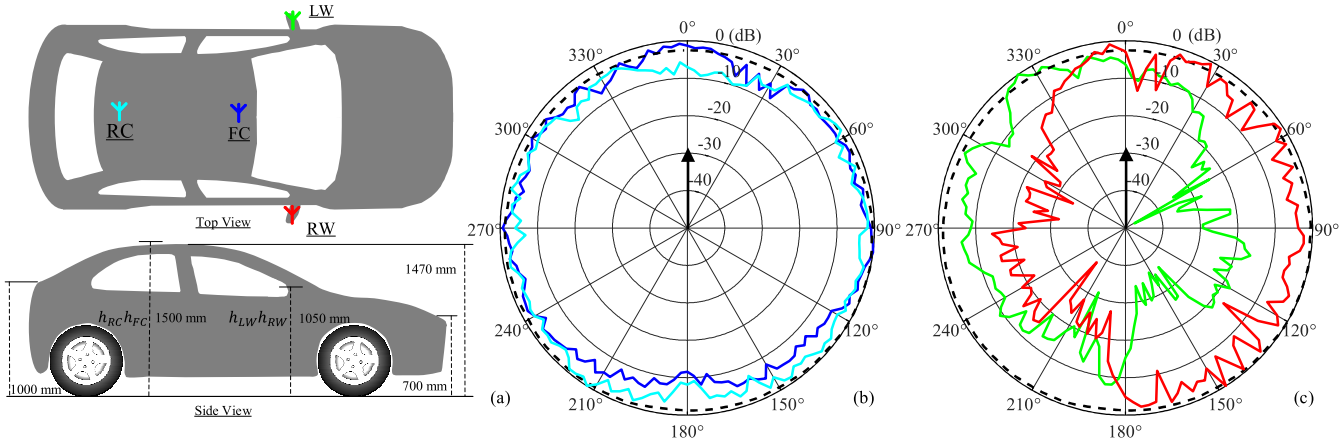


Fig. 2. (a) Illustration of the RX node positions on the FC and RC of the roof and on the LW and RW mirrors of the vehicle and their heights relative to the road, and (b) and (c) their measured azimuthal directivity patterns with the sleeve dipole antenna in free space (black dashed line), respectively. The upward arrow in (b) and (c) denotes the forward direction from the vehicle (note: the vehicle length is 4100 mm).

center (FC) and rear center (RC) of the roof and on the left-wing (LW) and right-wing (RW) mirrors of the vehicle. All RX antennas were mounted in a vertically polarized orientation. The roof-mounted RX nodes were secured directly onto the vehicle's body, however, due to the physical dimensions of the RX nodes, the base of the antenna maintained a distance of 30 mm from the roof surface. On the wing mirrors, to imitate the placement of the antenna inside the wing mirror unit while maximizing the signal coverage, the antenna was mounted on the outside edge of the wing mirror with the same type of dielectric spacer as used on the pedestrian's body.

The measured azimuthal antenna directivity patterns for the chest-mounted TX are shown in Fig. 1(b), and for the RX nodes mounted on the vehicle's roof and wing mirrors in Fig. 2(b) and (c), respectively, alongside the same sleeve dipole antenna in free space. The antenna directivity pattern for the pedestrian was measured using a single RX node that was placed on a nonconducting stand, situated at a distance of 10 m from the person's body. The RX node sampled the RSS at a rate of 1 kHz as the pedestrian uniformly rotated their body. The vehicle's directivity pattern was measured by moving a single TX node attached to a nonconducting stand around the vehicle at a radius of 10 m in 2.5° increments. At each angular increment, each of the RX nodes on the vehicle took a synchronized snapshot of 20 RSS measurements, which was then averaged in a postprocessing step. For both cases, the stand was set at a height that matched the chest region of the pedestrian and the measurements were performed in a large open field. From these directivity patterns, we can make the following observations; first, the presence of the pedestrian's body reduces the forward antenna directivity (i.e., in the forward half-plane) by as much as 12 dB. The directivity also decreases dramatically around the back of the pedestrian's body as a direct result of body shadowing. Second, the wing mirror antennas are subject to significant amounts of shadowing caused by the vehicle in the direction opposite to which they are mounted. Otherwise, they have a comparable directivity pattern to the roof positions on their unobstructed side. Last, the positioning of the roof antennas meant that they were also found to have a reduced antenna gain in the direction opposite to which they were mounted.

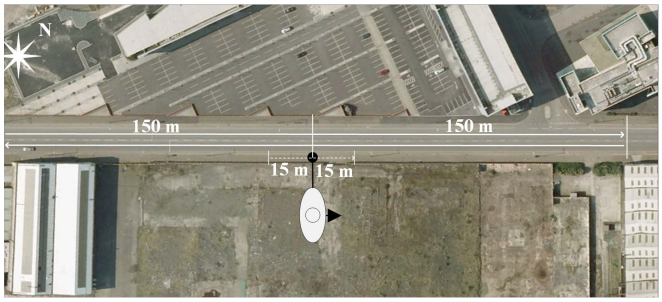


Fig. 3. Satellite view of the measurement environment showing the vehicle trajectories (white continuous lines with arrow heads) and pedestrian trajectory (white dashed line with arrow head) for the walking scenarios (note: image courtesy of Google Maps).

B. Measurement Environment and Scenarios

All of the measurements conducted in this paper were performed in the Titanic Quarter of Belfast, U.K. As shown in Fig. 3, the surrounding area contained a number of large office buildings situated at various distances and orientations relative to the roadside. This particular setup was chosen to isolate the effects of the vehicle and the pedestrian's body on the P2V channel. It is worth highlighting that further propagation effects can be straightforwardly superimposed on the proposed statistical channel model through the introduction of additional random variables. The scenarios were chosen to emulate some typical trajectories for both vehicles and pedestrians that may occur in this environment. As we can see from Fig. 3, the vehicle's trajectory was limited to the straight stretch of road, however, as is typical with urban environments vehicles may travel along the near side or the far side[1] of the road relative to the pedestrian. Furthermore,

[1]In the U.K., traffic laws stipulate that vehicles must travel on the left-hand lane of a single carriageway with two lanes. Furthermore, the speed limit is 13.4 ms^{-1} (or equivalently 30 mph) in an urban environment.

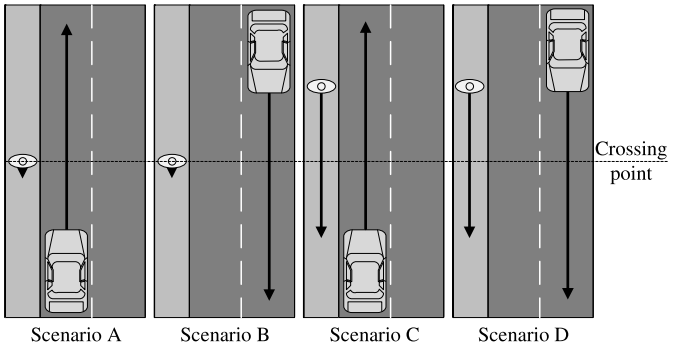


Fig. 4. Illustration of the pedestrian and vehicle trajectories during each scenario. It should be noted that the road is approximately 10 m in width and objects are not drawn to scale.

as the vehicle travels along the road, the pedestrian may adopt one of two states, namely, stationary or walking along the roadside. Therefore, as indicated in Fig. 4, four scenarios were considered.

1) The pedestrian stood *stationary* parallel to the roadside oriented *toward* the direction of the oncoming vehicle, which traveled on the side of the road *closest* to the pedestrian,
2) The pedestrian stood *stationary* parallel to the roadside oriented *away* from the direction of the oncoming vehicle, which traveled on the side of the road *furthest* from the pedestrian,
3) The pedestrian *walked* parallel to the roadside oriented *toward* the direction of the oncoming vehicle, which simultaneously traveled on the side of the road *closest* to the pedestrian, and,
4) The pedestrian *walked* parallel to the roadside oriented *away* from the direction of the oncoming vehicle, which simultaneously traveled on the side of the road *furthest* from the pedestrian.

It should be noted that, when the pedestrian was walking, he moved with an approximate velocity of 1.2 ms^{-1}, starting from a position 15 m behind the point in which he stood in the stationary scenarios, such that he would reach the stationary point when the vehicle passed by (as indicated by the dashed line in Fig. 4).

III. Path Loss And Large-Scale Fading

Fig. 5 shows the raw received signal power for three[2] of the RX nodes mounted on the vehicle as a function of the TX–RX distance obtained during Scenario A. As expected, the P2V channels experienced significant signal fluctuations, which varied according to the vehicle's position relative to the pedestrian. In particular, it was apparent that the channels underwent different fading conditions prior to, and after the vehicle passed the pedestrian. As a result of this observation, we segmented our data into two regions, namely, the *approaching* and *receding* regions. As the vehicle traversed into the receding region, the effect of the body-induced shadowing can be observed to cause an immediate reduction in the received signal power of the FC and LW channels [in excess of 20 dB, evident in the expanded view in Fig. 5(b)]. Moreover, the combined shadowing effect of both the pedestrian and the vehicle had an even more detrimental impact on the RW channel. Consequently, the fading that occurred within this region often extended into the noise floor at the extremities, and therefore we limited our data analysis beyond this point to a maximum distance (d_{max}) of 50 m behind the pedestrian for all scenarios. In vehicular communications, the antennas are typically mounted onto the highest point of the vehicle (i.e., the roof), to mitigate the severity of shadowing caused by the structure of the vehicle. As we can see in Fig. 5, the FC channel does in fact contain the highest received signal power in close proximity to the pedestrian. However, for the majority of the approaching region, the LW and RW channels, which are often omitted from consideration for V2V and V2I communications channels, were observed to contain a higher received signal power. This suggests that adopting a wing mirror-mounted antenna for use in P2V communications may also be valuable.

In the sequel, to understand the propagation mechanisms that effect P2V communications channels, we have decomposed the received signal power into its PL, large-scale (L), and small-scale (S) fading components. Using this approach, the received signal power can therefore be modeled by [37, eq. (2)]

$$P_r(dBm) = P_t(dBm) - \text{PL}(dB) - L(dB) - S(dB) \quad (1)$$

where P_t and P_r denote the TX and RX signal powers, respectively. To extract the PL and large-scale fading, the fluctuations in the received signal power due to small-scale fading were first removed. This was achieved by applying a smoothing window of 386 samples to the raw received signal power. The size of the window required was calculated based on the time it takes for the moving vehicle to pass through 10 wavelengths of the propagating signal.

Following the removal of the small-scale fading, it was observed for a small number of the P2V channels, in part of the approaching region, that the combined PL and large-scale fading fluctuations exhibited a noticeable quasi-periodicity. This artifact is usually indicative of a few strong signal paths (i.e., rays) interacting to cause constructive and destructive signal attenuations at the receive antenna. Typically, in vehicular communications channels, this phenomenon is modeled using the two-ray ground-reflection PL model [38], [39]. In this model, the received signal consists of two components: the LOS component that is just the transmitted signal propagating through free space, and a reflected component that is the transmitted signal reflected off the ground. Therefore, using the superposition of these two components, or rays, the two-ray ground-reflection PL, PL_{tr}, can be expressed as [40, eq. (2.12)]

$$\text{PL}_{tr}(dB) = 20\log_{10}\left(\frac{\lambda\sqrt{G_l}}{4\pi l} + \frac{\Gamma(\theta)\sqrt{G_r}\exp(j\Delta\phi)}{x+x'}\right) \quad (2)$$

where $\Delta\phi = 2\pi(x+x'-l)/\lambda$ is the phase difference between the two signal components, G_l and G_r are both a product

[2]The RC node was largely indistinguishable from the FC node when plotted on this scale, and has therefore been omitted for clarity.

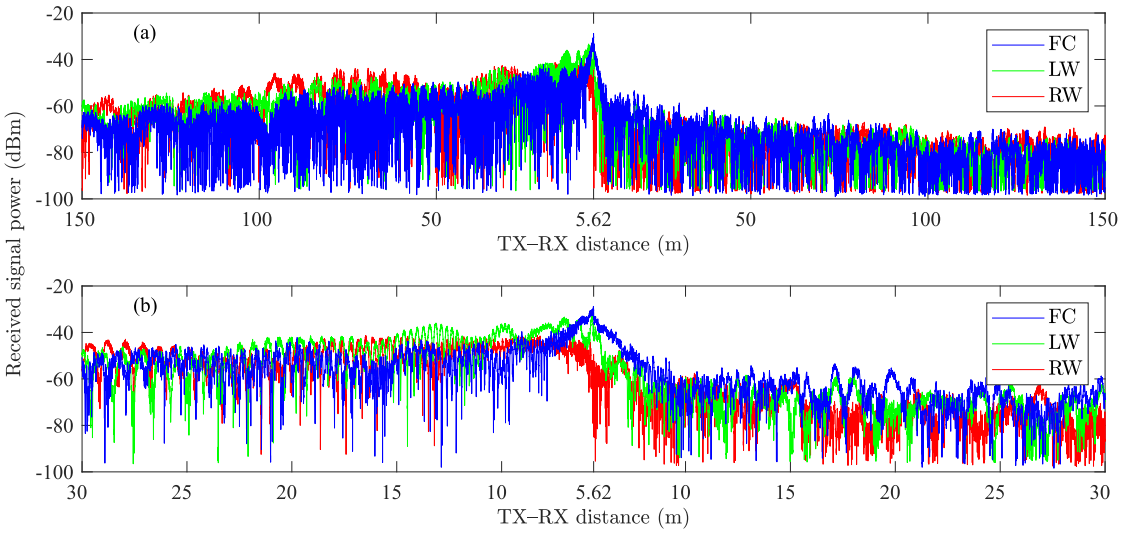


Fig. 5. (a) Received signal power as a function of TX–RX distance for the FC, LW mirror, and RW mirror channels for Scenario A. (b) Expanded view around the crossing point (note: minimum distance in this scenario is 5.62 m as labeled on the abscissa.)

of the TX and RX antenna gains for the LOS and reflected signal paths, which have a length l and $x + x'$, respectively. The ground-reflection coefficient, $\Gamma(\theta)$, with an incidence angle, θ, is calculated by $\Gamma(\theta) = (\sin\theta - z)/(\sin\theta + z)$ where $z = \sqrt{\epsilon_g - \cos^2\theta}$ for a horizontally polarized electromagnetic wave traveling across the road surface and ϵ_g is the dielectric constant of the ground.[3] The path lengths and reflection incidence angle can be geometrically derived as $l = \sqrt{d^2 - (h_t - h_r)^2}$, $x + x' = \sqrt{d^2 - (h_t + h_r)^2}$, and $\theta = \cos^{-1}(d/(x + x'))$, respectively, where d denotes the TX–RX distance and h_t and h_r are the TX and RX antenna heights, respectively.

As an example, Fig. 6 shows the two-ray ground-reflection PL model superimposed over the received signal power and combined PL and large-scale fading signal of the FC channel during Scenario A. To further assist with interpretation of this data, the transmit power has been removed so all the fading signals are now referenced relative to 0 dBm meaning they are synonymous with attenuation. As we can see, there are striking similarities between the combined signal fading and the model in the approaching region. This was hardly surprising, since the FC channel during this region maintained an optical LOS path with the chest-mounted TX along with an unobstructed view of the road surface between the vehicle and the pedestrian. However, as the vehicle neared the pedestrian and moments after passing them, the received signal power actually increased compared to what would normally be expected if considering free space propagation. This was a consistent observation throughout the measurement trials conducted in this paper and will likely be an important feature of future P2V channels. It is attributed to the strong enhancements caused by the vehicle's metallic structure, whereby signal contributions that may ordinarily be lost due to free space propagation are returned toward the RX node. The net result of this is an increase in the average received signal power. Furthermore, as the vehicle progressed through the receding region, where body shadowing becomes more prominent, it was evident that the two-ray ground-reflection model provides a poor approximation of the fading which occurred within this region. On a closer inspection of the combined PL and large-scale fading signal depicted in Fig. 6, a more frequent quasi-periodicity than predicted by the two-ray ground-reflection model was evident. This suggests that for this particular section of the FC channel, a higher order ray model could provide a better approximation of the PL. Moreover, in [42], it was reported that the two-ray ground-reflection model was better suited to rural areas and in other environments may be unreliable for distances less than 100 m, which aligns with our observations here for an urban environment. As a result, due to the inability of the two-ray ground-reflection model to accurately characterize the PL over all of the considered channels and all of their constituent regions (i.e., approaching and receding), we elected to adopt a more uniform and practical approach to modeling the PL, which is now detailed below.

The PL experienced in a fading channel can also be modeled in logarithmic form, such that the PL, PL(d), is given by [43, eq. (2)]

$$\mathrm{PL}(d) = \mathrm{PL}_0(d_0) + 10\eta \log_{10}\left(\frac{d}{d_0}\right), \quad d > d_0 \tag{3}$$

where d is the TX–RX distance in meters, $\mathrm{PL}_0(d_0)$ is the mean PL at the reference distance, d_0, and η is the PL exponent which is related to the propagation environment. In [36], it was found that using a linear (dual-slope) PL model for P2V channels significantly outperformed the traditional single-slope PL model approach. To emphasize this, the free space PL is also presented in Fig. 6, where, it can be seen that a calculation of the PL based on the free space model provides a poor overall fit to the measurement data. For this reason, in the sequel, we persist with the dual-slope PL model and denote

[3]The dielectric constant was chosen based on the empirical study presented in [41], which was measured under dry ($\epsilon_g = 0.34$) and wet ($\epsilon_g = 0.56$) road surface conditions with a TX frequency of 5.9 GHz.

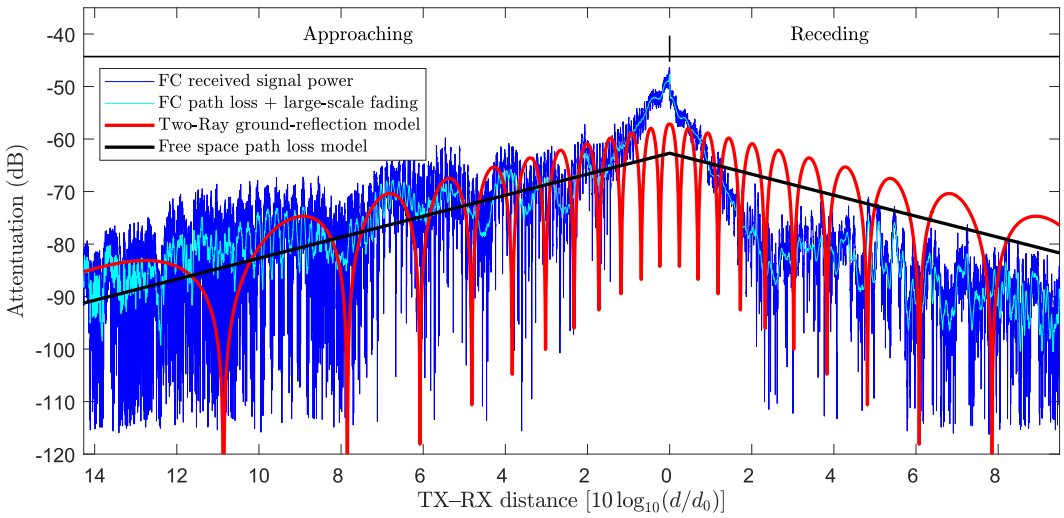


Fig. 6. Attenuation, extracted PL, and large-scale fading alongside the free-space path and two-ray ground-reflection PL models ($P_t = 0$ dBm, $G_t = G_r = 1$, $h_t = h_C = 1.2$ m, $h_r = h_{FC} = 1.5$ m, and $\epsilon_g = 0.34$) for the FC channel in Scenario A.

the sections (i.e., slopes) as *near* and *far* with respect to the pedestrian. Therefore, by applying these distance constraints in (3), the PL, PL(d), is now defined using a dual-slope PL model and is given by [19, eq. (2)]

$$\mathrm{PL}(d) = \begin{cases} \mathrm{PL}_0(d_0) + 10\eta_N \log_{10}\left(\dfrac{d}{d_0}\right), & d_0 \le d \le d_C \\ \mathrm{PL}_0\,(d_0) + 10\eta_N \log_{10}\left(\dfrac{d_C}{d_0}\right) & \\ \qquad + 10\eta_F \log_{10}\left(\dfrac{d}{d_C}\right), & d > d_C \end{cases} \tag{4}$$

where η_N and η_F are the PL exponents for the near and far regions, respectively, and d_C is the critical breakpoint distance, or simply breakpoint distance, which signifies the point where the data are segmented. The reference distance, d_0, must be large enough to ensure that only the far-field antenna characteristics are included in the PL model. In this analysis, as the vehicle passed the pedestrian at varying distances in each scenario,[4] we chose the minimum TX–RX distance for that scenario as the reference distance. To obtain the PL parameters in (4), linear regression was performed on the combined PL and large-scale fading signal with the logarithmically transformed TX–RX distance. There are a number of different techniques available to perform a linear regression analysis. In this paper, the `polyfit` function which is available in the Curve Fitting toolbox of MATLAB was used.

Prior to performing the model fitting, the combined signal must be segmented at the breakpoint distance, which is typically estimated as the first Fresnel distance, i.e., where the first Fresnel zone touches the ground [19]. However, due to the unique geometry of P2V channels, it was immediately evident that the optimal[5] breakpoint distance was significantly closer to the pedestrian. In [36], the breakpoint distance was selected visually where the fading was perceived to undergo drastically different variations in the received signal power. In this contribution, we improved on this process by estimating the breakpoint distance by jointly optimizing the near and far slopes simultaneously. This was achieved by incrementing the breakpoint distance (in steps of 0.05 m) from the minimum to the maximum distance within each region (i.e., $d_0 < d_C < d_{max}$), while performing linear regression for both slopes at each distance and recording the joint residual error. Thus, the breakpoint distance could be easily identified as the point where the combined regression error was lowest. It should be noted that the far slope linear regression fit was constrained at the breakpoint distance to ensure continuity of the PL model. As an example, Fig. 7 shows the combined PL and large-scale fading signal with the superimposed resultant estimated PL model for the FC channel in Scenario A. As we can see, this process of estimating the breakpoint distance provided an excellent fit to the combined PL and large-scale fading, which was superior to the single-slope and two-ray ground-reflection models (see Fig. 6).

The variation in the logarithmically transformed signal power due to large-scale, or equivalently shadowed fading, denoted as L, can be modeled as a Gaussian random variable, such that $L \sim N(u, v)$, where u and v denote the mean and standard deviation, respectively. Hence, by removing the estimated PL found in (4), the large-scale fading parameters within each section can be obtained using maximum likelihood estimation (MLE). The MLE method attempts to find the parameter values that maximize the likelihood function, given the observations. In this paper, we used the MLE function already available in the Statistics and Machine Learning Toolbox of MATLAB. Fig. 8 provides some example fits of the Gaussian distribution to the empirical densities of the large-scale fading for the FC channel. As we can see, the Gaussian distribution provides an excellent fit in both cases with some digression for the approaching far case [Fig. 8(a)].

[4]The minimum TX–RX distances varied due to the slightly different paths taken by the vehicle between scenarios.

[5]Using least-squares fitting, the optimality is determined in terms of the minimum sum of squared errors.

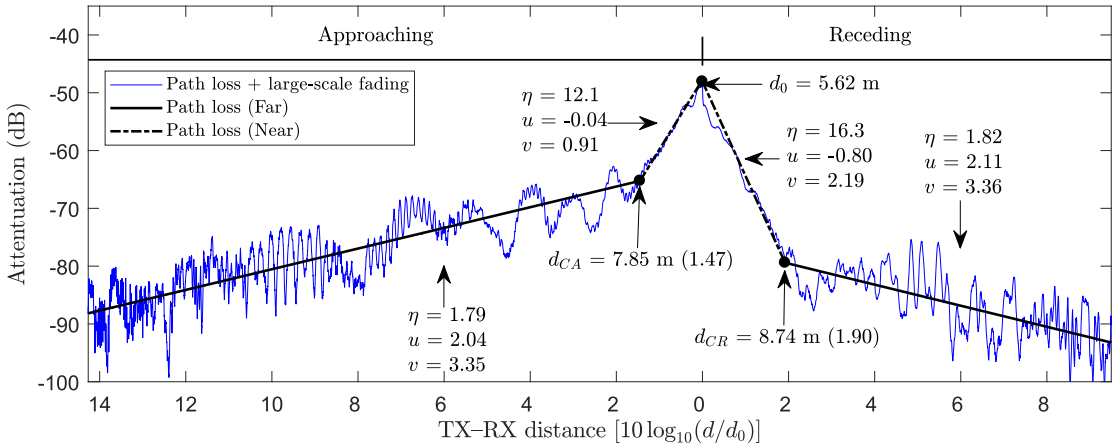


Fig. 7. Combined PL and large-scale fading with the superimposed estimated PL for the FC channel in Scenario A.

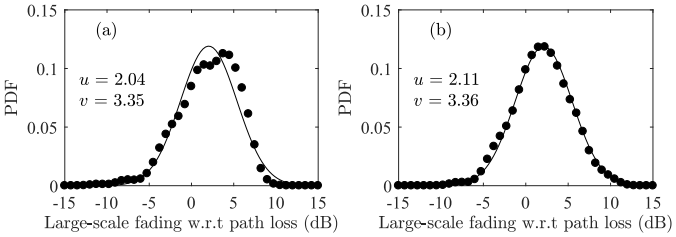


Fig. 8. PDFs of the empirical large-scale fading (black circles) with respect to PL and the Gaussian fits (black continuous lines) of the (a) approaching-far and (b) receding-far sections for the FC channel in Scenario A.

A. Stationary Pedestrian Oriented Toward Oncoming Vehicle (Scenario A)

The parameter estimates for the PL and large-scale fading for all scenarios are provided in Table I. In this scenario, the pedestrian was oriented toward the oncoming vehicle, and as a result, the approaching region contained no body-induced shadowing. From Table I, with the exception of the LW channel, the PL exponents between the approaching-far and -near regions showed significant disparity. In the approaching-far region, the PL exponents were reasonably close to those anticipated in free space, ranging from 1.53 to 2.18. However, when the vehicle entered the approaching-near region, the PL exponents obtained for the FC and RC mounted devices increased significantly, reflecting a rapid increase in the received signal power as the vehicle traveled closer to the pedestrian. As discussed previously, this observation was caused by the vehicle's metallic structure (hood and roof) returning a considerable amount of signal power in the direction of the pedestrian, that would ordinarily have been lost in a free space environment. As anticipated from the characteristics of the antenna directivity pattern depicted in Fig. 2(b), the PL exponent for the RW channel decreased at close proximity to the pedestrian as a result of a reduction in the received signal power caused by the increased shadowing of the direct signal path induced by the vehicle (reflected in the negative PL exponent obtained).

When the vehicle passed the pedestrian, it moved into the shadowed region behind the pedestrian's body. Similar to the approaching-near region, there was a substantial dropoff in the received signal power with distance (i.e., as the shadowing effect of the vehicle's structure on the direct signal path increased), while in the receding-far region (with the exception of the RW channel), the reduction in the received signal power was in line with that for the approaching-far region. Interestingly, although the LW channel contained no vehicle-induced shadowing for this scenario, the body-induced shadowing alone still resulted in a substantial power dropoff over the distance in the region directly behind the pedestrian's body. The increase in large-scale fading can be directly attributed to its position on the vehicle, which was located on its leftmost point (i.e., closest to the pedestrian), and thus would have moved through the most significantly shadowed region immediately behind the pedestrian's body. Over extended distances, as the vehicle progressed through the receding-far region, there may have been an increased opportunity for additional signal paths to reach the vehicle (e.g., due to reflections from the environment) that were not present immediately behind the pedestrian's body. Therefore, similar to the approaching case, there was an increase in the variation of the large-scale fading when moving from the receding-near to -far region (Table I). This increase was largely to be expected, as comparable V2V channels have been shown to be highly susceptible to strong ground reflections, which result in significant variations of the received signal power dependent on the distance and the elevation of the antennas [44].

B. Stationary Pedestrian Oriented Away From Oncoming Vehicle (Scenario B)

In an urban environment, traffic may flow in both directions; therefore, in this scenario, we considered the case were the vehicle moved in the opposite direction to that considered above. In direct contrast to Scenario A, the approaching and receding regions are now considered as NLOS and LOS, respectively. Most strikingly, the PL at the reference distance, with the exception of the RW channel, was significantly increased compared to Scenario A. For example, both the FC

TABLE I
PATH LOSS AND LARGE-SCALE FADING PARAMETER ESTIMATES FOR ALL SCENARIOS

Scenario	RX	Section: Approaching-Far				Approaching-Near					Receding-Near				Receding-Far		
		η_{AF}	u_{AF} (dB)	v_{AF} (dB)	d_{CA} (m)	η_{AN}	u_{AN} (dB)	v_{AN} (dB)	PL_0 (dB)	d_0 (m)	η_{RN}	u_{RN} (dB)	v_{RN} (dB)	d_{CR} (m)	η_{RF}	u_{RF} (dB)	v_{RF} (dB)
Stationary																	
A	FC	1.79	2.04	3.35	7.85	12.1	−0.04	0.91	47.8	5.62	16.3	−0.80	2.19	8.74	1.82	2.11	3.36
	RC	2.18	2.41	3.38	7.91	11.6	−0.37	1.39	48.2	5.62	33.6	0.38	2.96	6.84	2.11	1.95	3.27
	LW	1.87	1.03	3.78	12.0	1.72	1.07	2.80	56.3	5.62	23.6	−0.79	3.66	7.43	1.34	1.83	3.86
	RW	1.53	1.06	4.91	6.60	−27.0	2.58	2.74	59.8	5.62	3.32	2.40	3.49	13.5	0.90	1.53	4.05
B	FC	5.28	−0.07	6.57	10.7	1.57	0.39	1.00	60.7	6.10	2.89	−0.57	2.24	11.4	1.65	1.62	4.22
	RC	3.45	1.31	3.49	14.3	6.30	−0.59	4.38	57.9	6.10	4.02	−0.15	1.75	9.88	1.32	1.42	4.31
	LW	2.96	0.16	5.50	9.68	0.37	1.66	2.46	73.5	6.10	−8.44	2.40	2.35	9.57	1.15	1.08	4.28
	RW	1.71	0.60	4.74	15.1	4.09	0.51	4.20	62.0	6.10	−0.87	1.34	3.33	12.4	1.46	1.28	5.50
Walking																	
C	FC	1.41	1.90	3.44	10.5	7.02	−0.43	2.47	44.6	4.76	13.5	−0.64	2.76	8.95	1.38	2.24	2.94
	RC	1.59	2.72	3.19	21.4	5.00	0.85	3.12	45.0	4.76	29.0	0.13	3.72	6.42	1.12	2.07	3.15
	LW	1.62	0.80	4.82	22.3	1.81	2.23	2.93	54.3	4.76	12.8	0.07	4.50	7.82	0.61	2.53	3.43
	RW	1.41	0.96	5.67	5.67	−17.7	1.98	2.73	58.1	4.76	−2.17	2.80	2.44	5.98	2.57	0.86	5.35
D	FC	0.76	2.34	2.60	16.7	14.3	0.38	2.17	58.6	10.2	3.69	0.55	2.87	22.9	1.46	1.47	4.44
	RC	1.83	2.50	2.44	20.8	9.63	0.38	3.85	60.3	10.2	7.64	0.72	2.37	12.6	1.29	1.11	4.21
	LW	1.03	1.37	3.31	12.8	8.95	4.26	3.68	77.1	10.2	0.65	5.86	4.50	12.5	0.64	0.77	4.83
	RW	0.70	1.87	3.41	15.5	8.20	2.79	4.04	69.3	10.2	0.11	0.92	4.05	28.7	1.91	0.62	5.01

and RC channels experienced a greater than 10 dB increase in the PL at the reference distance (d_0), while the combined effect of the pedestrian's body and the vehicle's structure amplified this loss to over 17 dB for the LW-mounted device. This illustrates the deleterious impact that the pedestrian's body and the vehicle can have on the P2V channel when the optical path between the TX and the RX mounted an oncoming vehicle is blocked.

Compared to Scenario A, the PL exponents for the approaching-far region were greater, while in the approaching-near region, they were reduced. One possible explanation for this is due to the greater passing distance in this scenario (i.e., larger $d_{\min}$), as a result, the effect of the vehicle's structure on the received signal power was less pronounced. Nevertheless, similar to Scenario A, the severity of the fluctuation of the large-scale fading was also reduced when transitioning from the approaching-far to -near regions. Within the receding-near region, the RX nodes fitted to the vehicle were no longer subject to body shadowing, and with the exception of the FC device this acted to reduce the large-scale fading. It is worth highlighting that the wing mirror channels now experienced the opposite vehicular shadowing conditions to those faced during Scenario A (i.e., the RW channel had an unobstructed view of the pedestrian). Subsequently, this was the only channel for which abrupt changes in the received signal power (i.e., PL exponents) did not occur as the vehicle entered the receding-near region (Table I). In the receding-far region, the PL exponents were once again comparable to those expected for free space propagation (with exception to the RW channel), while variations in the large-scale fading increased presumably due to the increased influence of large-scale effects (e.g., additional opportunities for reflected waves from the surrounding environment) due to the extended distance.

C. Walking Pedestrian Oriented Toward Oncoming Vehicle (Scenario C)

To investigate the joint impact of pedestrian and vehicle movement, in this scenario, we considered the case where the pedestrian walked parallel to the roadside while maintaining the same orientation as in Scenario A. As we can see from Table I, this had a substantial impact on the breakpoint distance for the transition between the approaching-far and -near regions when compared to the equivalent stationary case (i.e., Scenario A). In general, the approaching-near region became larger when the person was mobile, suggesting that the influence of the body becomes more apparent at a larger distance than the stationary case. Overall, the PL exponents obtained for the approaching region for this scenario were lower than Scenario A. Contrasting the remainder of the channel parameters for the approaching-far and -near regions, we can see that they are largely comparable, with the exception of the large-scale fading observed by the LW and RW channels while in the approaching-far region, and the FC and RC devices while in the approaching-near region. In the approaching-far region, the lower mounted wing mirror devices would be more susceptible to strong ground reflections than the roof-mounted RX nodes. As the pedestrian walked, they introduced greater fluctuations in the received signal power evidenced by the increased variations in the large-scale fading (Table I). In the approaching-near region, the FC and RC channels now also become significantly affected by the motion of the user. As the vehicle's position at close proximity to the pedestrian is almost immediately to the left of the body (i.e., lateral to the torso),

all channels were vulnerable to quasi-LOS conditions as the pedestrian walked (e.g., the movement of the limbs).

When the vehicle transitioned into the shadowed region immediately behind the pedestrian, the breakpoint distances obtained were largely identical to the stationary case with the exception of the RW channel, which was significantly reduced compared to Scenario A. The majority of the PL exponents for the receding-near case were reduced slightly compared to Scenario A. Nonetheless, they were all still quite large confirming that there is a large dropoff in the received signal with distance in close proximity to the pedestrian. In the final segment of the vehicle's journey, the majority of the PL exponents were found to be less than that expected for free space, while the large-scale fading variations were found to be consistent with the stationary case. The exception to all of this was the RW channel which was particularly prone to the combined shadowing effect of the vehicle and the body (Table I).

D. Walking Pedestrian Oriented Away From Oncoming Vehicle (Scenario D)

From Table I, it was immediately evident that there was again a significant increase in the area covered by the approaching-near region compared to the equivalent stationary case. In addition to this, there was a dramatic increase in the PL exponents obtained when moving between the approaching-far and -near regions. The variation in the large-scale fading (with the exception of the FC channel) was also higher as the vehicle approached the pedestrian. These findings are consistent with the previous scenario, where the change in received signal power and variations in the large-scale fading were found to be greater in the region immediately behind the pedestrian due to the movement of the body. When the vehicle moved into the receding-near region, there was a noticeable increase in the variation of the large-scale fading compared to the stationary case due to the combined movement of the pedestrian and the vehicle. Within the receding-far region, the PL exponents and large-scale fading observed were comparable to Scenario B, suggesting that the movement of the pedestrian has less of an impact on the channel at greater distances to the vehicle.

IV. Small-Scale Fading

During our preliminary experiments, it became immediately evident that the P2V channel can experience fading conditions that are much worse than Rayleigh. In this setting, very few measurable scattered contributions are likely to have been detected, possibly because they extended below the sensitivity of the RX node. Instead, the small-scale fading will be the result of a superposition of a low number of direct and strong multipath components—propagation artifacts which strongly advocate the use of the κ-μ extreme distribution. The κ-μ extreme fading model was proposed in [45]–[47] as an extension to the κ-μ distribution to account for severe fading conditions. The κ-μ distribution intuitively comprises two fading parameters, κ which is simply a ratio of the total power of the dominant components (a^2) to the total power of the scattered waves ($2\mu s^2$), and μ which is related to the multipath clustering of the scattered waves [48]. The PDF, $f_R(r)$, of a fading signal envelope, R, which undergoes κ-μ fading is given as [45, eq. (11)]

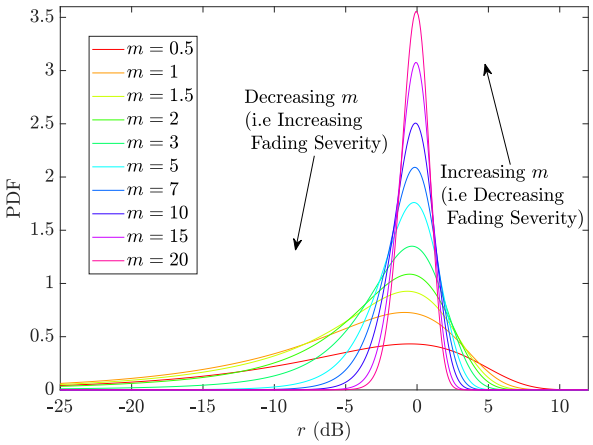


Fig. 9. κ-μ extreme PDF for increasing values of m with $\bar{r}$ equal to unity.

$$f_R(r) = \frac{2\mu(1+\kappa)^{\frac{\mu+1}{2}}}{\bar{r}\kappa^{\frac{\mu-1}{2}}\exp(\mu\kappa)}\left(\frac{r}{\bar{r}}\right)^{\mu} \times \exp\left[-\mu(1+\kappa)\left(\frac{r}{\bar{r}}\right)^2\right] I_{\mu-1}\left[2\mu\sqrt{\kappa(1+\kappa)}\frac{r}{\bar{r}}\right] \quad (5)$$

where $\bar{r}^2 = E[R^2]$ is the mean signal power (with $E[\cdot]$ denoting the expectation operator), $\bar{r}^2 = a^2 + 2\mu s^2$, and $I_n(\cdot)$ is the modified Bessel function of the first kind and order n. To obtain the κ-μ extreme distribution from the κ-μ distribution, the following relationship between κ, μ, and the Nakagami m parameter is used [46, eq. (2)]:

$$m = \frac{\mu(1+\kappa)^2}{1+2\kappa}. \quad (6)$$

By keeping m constant and allowing the κ and μ parameters to assume extreme values, i.e., $\kappa \to \infty$ (indicating a very strong LOS or dominant signal component) and $\mu \to 0$ (indicating very few multipaths), then with some mathematical manipulation, the PDF, $f_R(r)$, of a κ-μ extreme fading signal envelope, R, can be expressed as [46, eq. (4)]

$$f_R(r) = \frac{4m I_1\left(4m\frac{r}{\bar{r}}\right)}{\bar{r}\exp\left[2m\left(1+\left(\frac{r}{\bar{r}}\right)^2\right)\right]} + \exp(-2m)\delta\left(\frac{r}{\bar{r}}\right) \quad (7)$$

where $\delta(\cdot)$ is the Dirac delta function. For convenience and to aid with the interpretation of our results, Fig. 9 shows the κ-μ extreme PDF for increasing values of m. As we can see, as m increases the severity of fading is reduced, thus as m approaches infinity no fading occurs and the κ-μ extreme channel becomes deterministic. In this paper, the small-scale fading envelopes were obtained by removing the PL and large-scale fading calculated in Section II from the original received signal power and then converting the result to linear amplitude. All parameter estimates for the κ-μ extreme distribution were obtained using the `lsqnonlin` function available in the optimization toolbox of MATLAB. This function solves nonlinear least-squares curve

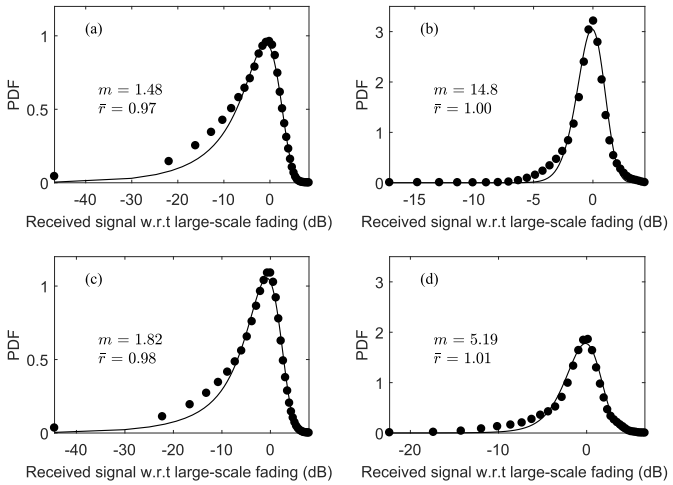


Fig. 10. PDFs of the empirical small-scale fading (black circles) and the κ-μ extreme distribution (black continuous lines) with respect to large-scale fading of the FC channel for the (a) approaching-far and (b) approaching-near regions in Scenario A (i.e., stationary pedestrian) and (c) and (d) approaching-far and (b) approaching-near regions in Scenario C (i.e., walking pedestrian).

fitting problems with the added benefit of being able to add constraints to the model parameters. Using the PDF for the κ-μ extreme distribution, the residual error between the measured data and the proposed fit given initial model parameters is computed. This process is then repeated with each iteration choosing parameter values, which reduce the residual error, concluding when the parameters with the best fit (i.e., lowest residual error) are obtained [49]. To improve the likelihood of obtaining the best fit overall, the entire model fitting process was performed using numerous initial start positions, obtained using the `multistart` function of MATLAB. To evaluate the accuracy of the model fitting, the normalized mean square error (NMSE) was computed and is provided along with the parameter estimates in Table II. As we can see, the NMSE values indicate that the κ-μ extreme model provided a good fit to the measurement data for the majority of the considered channels (NMSE > 0.96).[6]

A. Stationary Pedestrian Oriented Toward Oncoming Vehicle (Scenario A)

Within the approaching-far region, the roof-mounted devices suffered most from small-scale signal fluctuations as indicated by the estimated m values (Table II). Signal components generated by the metal bodywork of the vehicle, in particular, the engine compartment (i.e., hood) for the FC device and the slight curvature of the roof in the case of the RC device are likely to have contributed to the more significant fading observed at these locations. For the wing mirror-mounted devices, which were always in LOS of the body worn TX, it was evident from the m parameters that both underwent less fading when compared to the roof-positioned antennas (Table II). As an example of the model fitting process, Fig. 10(a) shows the empirical PDF for the FC-mounted RX node compared with the κ-μ extreme distribution. As we can see, the κ-μ extreme distribution provides an excellent fit to the empirical data for all fades until the -10 dB level, with some slight deviation below this point. As the vehicle progressed along its trajectory into the approaching-near region, the shorter transmission distance provided an opportunity for an increase in the dominance of the LOS signal component resulting in a significant rise in the values of the estimated m parameters (Table II) and a reduction in the depth of the fades. Of course, the exception to this was the RW channel, which now became partially shadowed by the vehicle causing greater small-scale variations of the received signal. Fig. 10(b) depicts the distribution of the empirical data for the FC channel in this region, which we can see is almost symmetrical in nature representing an equivalent number of upfade and downfade from the large-scale signal level. Again, the agreement between the empirical data and the κ-μ extreme distribution is found to be very good.

Despite the body shadowing that occurred immediately behind the pedestrian, when the vehicle entered the receding-near region, nearly all of the links saw a reduction in the variation of their small-scale fading. This observation must be tempered with the more significant variation in the large-scale fading when moving from the approaching-near region into the receding-near region (Table I). The RW channel saw a slight increase in the variation of the small-scale fading due to the double-shadowing condition now caused by the pedestrian's body and the structure of the vehicle, as both obscured the optical signal path. However, again the bulk of the fluctuation occurred in the large-scale fading suggesting that shadowing is more pronounced in the large-scale sense.

As expected, in the receding-far region, the estimated m values were once again reduced suggesting an increase in the intensity of the small-scale fading. Nonetheless, despite the increase in the distance between the TX and RX, which ordinarily would have been expected to provide the opportunity for the generation of an increased number multipath components (including scattering), a separate analysis undertaken by the authors using the κ-μ distribution (not reported here for brevity), indicated extremely high κ ($\kappa > 102$) and low μ values ($\mu \to 0$). At first glance, this result may seem surprising, however considering the intrinsic nature of κ-μ extreme fading, this observation may have been due to the fact that any scattered signal contributions arriving at the RX may have extended below the minimum detectable power level. As the bespoke RX nodes used in this paper were based on repurposed, commercially available, transceiver chipsets, this type of fading is likely to be a realistic characteristic of future P2V communications.

B. Stationary Pedestrian Oriented Away From Oncoming Vehicle (Scenario B)

In the approaching-far region of Scenario B, the estimated m parameters obtained were most comparable with those recorded for the receding-far region of Scenario A, presumably due to the symmetry of the propagation geometry. As the vehicle neared the pedestrian, although the channels were still subject to body-induced shadowing, the m parameters increased,

[6] A value of unity indicates a perfect fit.

TABLE II
κ-μ EXTREME PARAMETER ESTIMATES AND NMSE FOR ALL SCENARIOS

		Section											
		Approaching-Far			Approaching-Near			Receding-Near			Receding-Far		
Scenario	RX	$\hat{m}$	$\hat{\bar{r}}$	NMSE	$\hat{m}$	$\hat{\bar{r}}$	NMSE	$\hat{m}$	$\hat{\bar{r}}$	NMSE	$\hat{m}$	$\hat{\bar{r}}$	NMSE
						Stationary							
A	FC	1.48	0.97	0.986	14.8	1.00	0.975	12.2	1.00	0.961	1.53	0.94	0.994
	RC	1.17	0.94	0.967	14.9	1.00	0.984	22.7	1.00	0.988	1.59	0.95	0.996
	LW	3.68	1.01	0.985	9.70	1.00	0.985	7.72	0.98	0.936	1.91	0.98	0.967
	RW	3.56	1.00	0.974	1.93	0.96	0.980	1.63	0.96	0.981	2.07	0.97	0.990
B	FC	1.40	0.94	0.998	12.5	1.00	0.997	3.05	1.01	0.993	2.39	0.99	0.984
	RC	1.05	0.91	0.937	5.36	1.00	0.983	3.17	1.03	0.979	3.05	0.99	0.962
	LW	1.78	0.97	0.988	3.36	1.00	0.988	1.12	0.94	0.960	2.29	1.00	0.968
	RW	2.18	0.99	0.955	4.18	1.00	0.987	1.87	1.04	0.965	5.66	1.00	0.969
						Walking							
C	FC	1.82	0.98	0.990	5.19	1.01	0.973	9.62	1.00	0.948	1.27	0.93	0.978
	RC	1.15	0.93	0.966	2.08	1.01	0.897	20.8	0.99	0.986	1.47	0.96	0.986
	LW	3.56	1.00	0.968	4.36	1.03	0.954	4.84	1.00	0.928	1.37	0.94	0.991
	RW	4.27	1.00	0.973	2.79	0.98	0.982	1.17	0.95	0.912	1.46	0.95	0.991
D	FC	1.24	0.93	0.979	4.61	1.00	0.939	2.91	1.01	0.974	3.59	1.00	0.978
	RC	1.14	0.91	0.971	2.40	0.99	0.975	4.63	1.02	0.964	5.54	1.00	0.943
	LW	1.63	0.97	0.990	1.58	0.98	0.986	1.54	0.97	0.988	2.72	1.00	0.980
	RW	1.71	0.98	0.984	2.20	0.99	0.973	5.63	1.00	0.965	8.34	1.00	0.983

although not as a significantly as observed in Scenario A. Interestingly, as the vehicle continued into the receding-near region, the *m* parameters suggest greater small-scale fading occurred than during the approaching-near region. One plausible explanation for this observation was due to an increased opportunity for destructive interference caused by additional signal components that were previously filtered due to the shielding effect of the body. During the final stages of the vehicle's journey, greater variation in the small-scale fading was once again observed (Table II). In line with the observations from the previous scenario, the wing mirror channel which was not subject to vehicle-induced shadowing (i.e., the RW channel in this case) underwent the least amount of fading at the extremities.

C. Walking Pedestrian Oriented Toward Oncoming Vehicle (Scenario C)

Upon first observation, the estimated *m* parameters obtained for this scenario appeared comparable to the equivalent stationary case (i.e., Scenario A). However, while this was certainly true for the far regions [Fig. 10(a) and (c)], this was not the case for the near zones [Fig. 10(b) and (d)]. Indeed, the most notable changes occurred when the vehicle was within close proximity to the now mobile pedestrian, where the estimated *m* values were now reduced compared to the equivalent stationary case (Table II). Clearly, the disruption introduced into the channel by the pedestrian's mobility (e.g., movement of the limbs) created increased volatility in the small-scale fading. This can be visualized in Fig. 10(d), where the FC channel during the approaching-near region contained a greater number of fades below the -5 dB level than during the stationary case [Fig. 10(b)]. As the vehicle receded further away from the pedestrian, the impact of the person's mobility appeared to be less prominent than before, with estimated *m* parameters reducing to values marginally lower than those obtained when the pedestrian was stationary.

D. Walking Pedestrian Oriented Away From Oncoming Vehicle (Scenario D)

During the approaching-far region of Scenario D, as before, the estimated *m* values were comparable to the stationary case (Scenario B, Table II). Again, the impact of pedestrian mobility on the P2V channel is most pronounced when the vehicle and pedestrian are in close proximity of one another (i.e., approaching- and receding-near regions). In line with what was observed in Scenario C, the mobility of the pedestrian generally caused an increase in the intensity of the small-scale fading and a corresponding reduction the estimated *m* parameters (Table II). Most surprisingly though there was a slight increase in the *m* values obtained for all channels in the receding-far region of Scenario D. However, as we can see from Fig. 9, the variation in the *m* parameter between the corresponding channels in Scenarios B and D does not have a significant impact on the overall small-scale fading conditions.

V. CONCLUSION

In this paper, the pedestrian-to-vehicle communication channel has been investigated within an urban environment at 5.8 GHz. It was found that the P2V channel underwent significant signal fluctuations, which noticeably varied depending on the position of the vehicle relative to the pedestrian. Additionally, it was found that the two-ray ground-reflection PL model, often used to characterize the signal attenuation in vehicular communications channels, was not suited for modeling the fading conditions experienced in P2V channels. Instead, the PL was best described using a dual-slope PL model, which enabled us to distinguish between different PL characteristics experienced at close proximity to the pedestrian and further away. The breakpoint distance was dependent on the position of the RX, which occurred at much shorter distances than those typically considered for other V2X applications. In all cases, the logarithmically transformed large-scale fading was found to be well modeled as a Gaussian random variable.

Due to the often extreme nature of the small-scale fading which can occur in P2V communication channels, we have utilized the κ-μ extreme distribution to model its behavior. It was observed that when the pedestrian is stationary and within close proximity to the vehicle, the small-scale fading is typically reduced compared to the case when the vehicle is further away. When the pedestrian became mobile, while the small-scale fading observed at the extremities remained largely unperturbed, at reduced distances, the impact of the mobility of both ends of the wireless link had a more discernible effect. Surprisingly, in some scenarios, the often omitted wing mirror channels were found to suffer less fading than the roof-mounted antennas, suggesting that adopting a wing mirror-mounted antenna for use in P2V communications may also be valuable. Finally, it is worth remarking that using the simulation technique proposed in [50] for producing κ-μ extreme random variables, along with the straightforward generation of the Gaussian large-scale fading and computation of the PL, the results presented in this paper can readily be reproduced for incorporation into ITS network simulations.

REFERENCES

[1] P. S. Hall and Y. Hao, "Antennas and propagation for body centric communications," in *Proc. 1st Eur. Conf. Antennas Propag. (EuCAP)*, Nice, France, Nov. 2006, pp. 1–7.

[2] D. S. Yang, "A new radio propagation model at 2.4 GHz for wireless medical body sensors in outdoor environment," in *Proc. 35th Annu. Int. Conf. IEEE Eng. Med. Biol. Soc. (EMBC)*, Osaka, Japan, Jul. 2013, pp. 3269–3273.

[3] G. Araniti, C. Campolo, M. Condoluci, A. Iera, and A. Molinaro, "LTE for vehicular networking: A survey," *IEEE Commun. Mag.*, vol. 51, no. 5, pp. 148–157, May 2013.

[4] C. F. Mecklenbrauker *et al.*, "Vehicular channel characterization and its implications for wireless system design and performance," *Proc. IEEE*, vol. 99, no. 7, pp. 1189–1212, Jul. 2011.

[5] A. Paier, L. Bernadó, J. Karedal, O. Klemp, and A. Kwoczek, "Overview of vehicle-to-vehicle radio channel measurements for collision avoidance applications," in *Proc. IEEE 71st Veh. Technol. Conf.*, Taipei, Taiwan, May 2010, pp. 1–5.

[6] H. Wu *et al.*, "An empirical study of short range communications for vehicles," in in *Proc. ACM VANET*, New York, NY, USA: ACM Press, 2005, pp. 83–84.

[7] C. Wietfeld, "Performance evaluation of vehicle-roadside communication systems in shadowing and multipath fading environments," in *Proc. IEEE Veh. Technol. Conf.*, Chicago, IL, USA, Jul. 1995, pp. 947–952.

[8] C.-X. Wang, X. Cheng, and D. I. Laurenson, "Vehicle-to-vehicle channel modeling and measurements: Recent advances and future challenges," *IEEE Commun. Mag.*, vol. 47, no. 11, pp. 96–103, Nov. 2009.

[9] G. Acosta-Marum and M. A. Ingram, "Six time- and frequency-selective empirical channel models for vehicular wireless LANs," in *Proc. IEEE 66th Veh. Technol. Conf. (VTC Fall)*, Baltimore, MD, USA, Sep. 2007, pp. 2134–2138.

[10] X. Wu *et al.*, "Vehicular communications using DSRC: Challenges, enhancements, and evolution," *IEEE J. Sel. Areas Commun.*, vol. 31, no. 9, pp. 399–408, Sep. 2013.

[11] Y. Hu, W. Zhang, Y. Li, and P. Xiong, "The research of WAVE architecture based vehicles to vehicles communication technology of intelligent transport system," in *Proc. Int. Conf. Power Electron. Intell. Transp. Syst. (PEITS)*, Shenzhen, China, Dec. 2009, pp. 134–139.

[12] M. Boban, R. Meireles, J. Barros, P. Steenkiste, and O. K. Tonguz, "TVR—Tall vehicle relaying in vehicular networks," *IEEE Trans. Mobile Comput.*, vol. 13, no. 5, pp. 1118–1131, May 2014.

[13] H.-R. Chuang, "Human operator coupling effects on radiation characteristics of a portable communication dipole antenna," *IEEE Trans. Antennas Propag.*, vol. 42, no. 4, pp. 556–560, Apr. 1994.

[14] S. L. Cotton, A. McKernan, A. J. Ali, and W. G. Scanlon, "An experimental study on the impact of human body shadowing in off-body communications channels at 2.45 GHz," in *Proc. 5th Eur. Conf. Antennas Propag. (EUCAP)*, Rome, Italy, Apr. 2011, pp. 3133–3137.

[15] S. L. Cotton, W. G. Scanlon, and A. McKernan, "Improving signal reliability in outdoor body-to-body communications using front and back positioned antenna diversity," in *Proc. IEEE 6th Eur. Conf. Antennas Propag. (EUCAP)*, Prague, Czech Republic, Mar. 2012, pp. 3393–3396.

[16] M. Walter, U. C. Fiebig, and A. Zajic, "Experimental verification of the non-stationary statistical model for v2v scatter channels," in *Proc. IEEE 80th Veh. Technol. Conf. (VTC Fall)*, Vancouver, BC, Canada, Sep. 2014, pp. 1–5.

[17] T. Abbas, F. Tufvesson, K. Sjöberg, and J. Karedal. (Mar. 2012). "Measurement based shadow fading model for vehicle-to-vehicle network simulations." [Online]. Available: https://arxiv.org/abs/1203.3370

[18] C. Sommer, S. Joerer, M. Segata, O. K. Tonguz, R. L. Cigno, and F. Dressler, "How shadowing hurts vehicular communications and how dynamic beaconing can help," in *Proc. IEEE INFOCOM*, Turin, Italy, Apr. 2013, pp. 110–114.

[19] L. Cheng, B. E. Henty, D. D. Stancil, F. Bai, and P. Mudalige, "Mobile vehicle-to-vehicle narrow-band channel measurement and characterization of the 5.9 GHz dedicated short range communication (DSRC) frequency band," *IEEE J. Sel. Areas Commun.*, vol. 25, no. 8, pp. 1501–1516, Oct. 2007.

[20] S. Kaul *et al.*, "Effect of antenna placement and diversity on vehicular network communications," in *Proc. 4th Annu. IEEE Commun. Soc. Conf. Sensor, Mesh Ad Hoc Commun. Netw.*, San Diego, CA, USA, Jun. 2007, pp. 112–121.

[21] L. Reichardt, T. Fugen, and T. Zwick, "Influence of antennas placement on car to car communications channel," in *Proc. 3rd Eur. Conf. Antennas Propag. (EUCAP)*, Berlin, Germany, Mar. 2009, pp. 630–634.

[22] D. Kornek, M. Schack, E. Slottke, O. Klemp, I. Rolfes, and T. Kurner, "Effects of antenna characteristics and placements on a vehicle-to-vehicle channel scenario," in *Proc. Int. Conf. Commun. Workshops*, Capetown, South Africa, May 2010, pp. 1–5.

[23] R. L. Jesch, "Measured vehicular antenna performance," *IEEE Trans. Veh. Technol.*, vol. VT-34, no. 2, pp. 97–107, May 1985.

[24] M. Mackowiak and L. M. Correia, "Towards a radio channel model for off-body communications in a multipath environment," in *Proc. 18th Eur. Wireless Conf. Eur. Wireless (EW)*, Poznań, Poland, Apr. 2012, pp. 1–7.

[25] K. David and A. Flach, "Car-2-X and pedestrian safety," *IEEE Veh. Technol. Mag.*, vol. 5, no. 1, pp. 70–76, Mar. 2010.

[26] L. Chen and C. Englund, "Cooperative intersection management: A survey," *IEEE Trans. Intell. Transp. Syst.*, vol. 17, no. 2, pp. 570–586, Feb. 2016.

[27] S. Hisaka and S. Kamijo, "On-board wireless sensor for collision avoidance: Vehicle and pedestrian detection at intersection," in *Proc. 14th Int. IEEE Conf. Intell. Transp. Syst. (ITSC)*, Washington, DC, USA, Oct. 2011, pp. 198–205.

[28] Y. Sawa, T. Kitani, N. Shibata, K. Yasumoto, and M. Ito, "A method for pedestrian position estimation using inter-vehicle communication," in *Proc. IEEE GLOBECOM Workshops*, New Orleans, LO, USA, Dec. 2008, pp. 1–6.

[29] J. J. Anaya, P. Merdrignac, O. Shagdar, F. Nashashibi, and J. E. Naranjo, "Vehicle to pedestrian communications for protection of vulnerable road users," in *Proc. IEEE Intell. Vehicles Symp.*, Lansing, MI, USA, Jun. 2014, pp. 1037–1042.

[30] P. Merdrignac, O. Shagdar, I. B. Jemaa, and F. Nashashibi, "Study on perception and communication systems for safety of vulnerable road users," in *Proc. 18th IEEE Int. Conf. Intell. Transp. Syst. (ITSC)*, Las Palmas, Spain, Sep. 2015, pp. 1876–1881.

[31] X. Wu *et al.*, "Cars talk to phones: A DSRC based vehicle-pedestrian safety system," in *Proc. IEEE 80th Vehicular Technol. Conf. (VTC Fall)*, Vancouver, BC, Canada, Sep. 2014, pp. 1–7.

[32] M. A. Abid, O. Chakroun, and S. Cherkaoui, "Pedestrian collision avoidance in vehicular networks," in *Proc. IEEE Int. Conf. Commun. (ICC)*, Budapest, Hungary, Jun. 2013, pp. 2928–2932.

[33] Y. Ibdah and Y. Ding, "Mobile-to-mobile channel measurements at 1.85 GHz in suburban environments," *IEEE Trans. Commun.*, vol. 63, no. 2, pp. 466–475, Feb. 2015.

[34] M. G. Doone and S. L. Cotton, "First-order characteristics of the person-to-vehicle channel at 5.8 GHz," in *Proc. 8th Eur. Conf. Antennas Propag. (EuCAP)*, The Hague, The Netherlands, Apr. 2014, pp. 848–851.

[35] M. G. Doone and S. L. Cotton, "A statistical analysis of person-to-vehicle communications channels in an urban environment at 5.8 GHz," in *Proc. USNC-URSI Radio Sci. Meeting (Joint AP-S Symp.)*, Memphis, TN, USA, Jul. 2014, p. 236.

[36] M. G. Doone and S. L. Cotton, "Fading characteristics of dynamic person-to-vehicle channels at 5.8 GHz," in *Proc. 9th Eur. Conf. Antennas Propag. (EuCAP)*, Lisbon, Portugal, Apr. 2015, pp. 1–5.

[37] N. Perpinias, A. Palaios, J. Riihijarvi, and P. Mahonen, "Impact of the path loss model on the spatial structure of shadow fading," in *Proc. IEEE Int. Conf. Commun. (ICC)*, Sydney, NSW, Australia, Jun. 2014, pp. 5871–5877.
[38] C. Sommer and F. Dressler, "Using the right Two-Ray model? A measurement based evaluation of PHY models in VANETs," in *Proc. ACM MobiCom*, 2011, pp. 1–3.
[39] C. Sommer, S. Joerer, and F. Dressler, "On the applicability of Two-Ray path loss models for vehicular network simulation," in *Proc. IEEE Veh. Netw. Conf. (VNC)*, Nov. 2012, pp. 64–69.
[40] A. Goldsmith, *Wireless Communications*. Cambridge, U.K.: Cambridge Univ. Press, 2005.
[41] M. González-Domínguez, D. Bao, S. Dadín, I. Cuiñas, and M. G. Sánchez, "Measuring *in-situ* reflection coefficients due to road pavements at 5.9 GHz," *Electron. Lett.*, vol. 52, no. 25, pp. 2072–2074, 2016.
[42] B. Kihei, J. A. Copeland, and Y. Chang, "Improved 5.9 GHz V2V short range path loss model," in *Proc. IEEE 12th Int. Conf. Mobile Ad Hoc Sensor Syst. (MASS)*, Oct. 2015, pp. 244–252.
[43] H. Kremo, K. Nakagawa, O. Altintas, H. Tanaka, and T. Fujii, "Characterization of first and second order statistics of large scale fading using vehicular sensors," in *Proc. IEEE 81st Veh. Technol. Conf. (VTC Spring)*, Glasgow, U.K., May 2015, pp. 1–5.
[44] S. Oh, S. Kaul, and M. Gruteser, "Exploiting vertical diversity in vehicular channel environments," in *Proc. 20th Int. Symp. Pers., Indoor Mobile Radio Commun.*, Toyko, Japan, Sep. 2009, pp. 958–962.
[45] M. Yacoub, "The κ-μ distribution and the η-μ distribution," *IEEE Antennas Propag. Mag.*, vol. 49, no. 1, pp. 68–81, Feb. 2007.
[46] G. S. Rabelo, U. S. Dias, and M. D. Yacoub, "The κ-μ extreme distribution: Characterizing severe fading conditions," in *IEEE MTT-S Int. Microw. Symp. Dig.*, Belem, Brazil, Nov. 2009, pp. 244–248.
[47] G. S. Rabelo and M. D. Yacoub, "The κ-μ extreme distribution," *IEEE Trans. Commun.*, vol. 59, no. 10, pp. 2776–2785, Oct. 2011.
[48] S. L. Cotton, "Human body shadowing in cellular device-to-device communications: Channel modeling using the shadowed κ-μ fading model," *IEEE J. Sel. Areas Commun.*, vol. 33, no. 1, pp. 111–119, Jan. 2015.
[49] T. F. Coleman and Y. Li, "An interior trust region approach for nonlinear minimization subject to bounds," *SIAM J. Optim.*, vol. 6, no. 2, pp. 418–445, 1996.
[50] F. J. Lopez-Martinez, L. Moreno-Pozas, and E. Martos-Naya, "Novel results for the κ-μ extreme fading distribution: Generation of white samples and capacity analysis," *IEEE Commun. Lett.*, vol. 19, no. 9, pp. 1580–1583, Sep. 2015.



Michael G. Doone (M'18) received the M.Eng. degree (Hons.) in electrical and electronic engineering from Queen's University Belfast, Belfast, U.K., in 2013, where he is currently pursuing the Ph.D. degree, with a focus on wireless vehicular communications channels involving people.

His current research interests include the characterization and modeling of wireless vehicular fading channels involving people, for both terrain-based and unmanned aerial vehicles, through bespoke test-bed systems and channel measurements.



Simon L. Cotton (S'04–M'07–SM'14) received the B.Eng. degree in electronics and software from Ulster University, U.K., in 2004, and the Ph.D. degree in electrical and electronic engineering from Queen's University Belfast, Belfast, U.K., in 2007.

He is currently the Director of the Centre for Wireless Innovation, Queen's University Belfast. He has authored or co-authored over 140 publications in major IEEE/IET journals and refereed international conferences and two book chapters. He holds two patents. His current research interests include cellular device-to-device, vehicular, body-centric communications, radio channel characterization and modeling, and the simulation of wireless channels.

Dr. Cotton was a recipient of the H. A. Wheeler Prize, in 2010, from the IEEE Antennas and Propagation Society for the best applications journal paper in the IEEE TRANSACTIONS ON ANTENNAS AND PROPAGATION in 2009 and the Sir George Macfarlane Award, in 2011, from the U.K. Royal Academy of Engineering in recognition of his technical and scientific attainment since graduating from his first degree in engineering.

David W. Matolak (S'82–M'83–SM'00) received the B.S. degree from Pennsylvania State University, University Park, PA, USA, the M.S. degree from the University of Massachusetts, Amherst, MA, USA, and the Ph.D. degree from The University of Virginia, Charlottesville, VA, USA, all in electrical engineering.

He has over 20 years of experience in communication system research, development, design, and deployment, with private companies, government institutions, and academia, including AT&T Bell Labs, L3 Communication Systems, Salt Lake City, UT, USA, MITRE, Bedford, MA, USA, and Lockheed Martin, Bethesda, MD, USA. Since 2012, he has been a Professor with the University of South Carolina, Columbia, SC, USA. He has authored or co-authored more than 200 publications and has eight patents. His research interests include radio channel modeling and communication techniques for non-stationary fading channels.

Dr. Matolak is a member of Eta Kappa Nu, Sigma Xi, Tau Beta Pi, URSI, ASEE, and AIAA.



Claude Oestges (F'16) received the M.Sc. and Ph.D. degrees in electrical engineering from the Université catholique de Louvain (UCL), Louvain-la-Neuve, Belgium, in 1996 and 2000, respectively.

In 2001, he joined the Smart Antennas Research Group (Information Systems Laboratory), Stanford University, Stanford, CA, USA, as a Post-Doctoral Scholar. From 2002 to 2005, he was with the Microwave Laboratory, UCL, as a Post-Doctoral Fellow of the Belgian Fonds de la Recherche Scientifique (FRS-FNRS). He is currently a Full Professor with the Electrical Engineering Department, Institute for Information and Communication Technologies, Electronics and Applied Mathematics, UCL. He has authored or co-authored over three books and more than 200 journal papers and conference communications.

Dr. Oestges has been the Chair of COST Action CA15104 IRACON since 2016. He was a recipient of the 1999–2000 IET Marconi Premium Award and the IEEE Vehicular Technology Society Neal Shepherd Award in 2004 and 2012.

Sean F. Heaney, photograph and biography not available at the time of publication.



William G. Scanlon (M'98–SM'13) received the Ph.D. degree from Ulster University, Coleraine, U.K., in 1997.

In 1998, he was a Lecturer with Ulster University. He was a Senior Lecturer and a Full Professor (Wireless Communications) with Queen's University Belfast, Belfast, U.K., in 2002 and 2008, respectively, where he served as the Research Director for Wireless Communication Systems, the Director of the Centre for Wireless Innovation, and the Head of School of Electronics, Electrical Engineering and Computer Science from 2002 to 2018. He also held a Part-Time Chair in short-range radio at the University of Twente, Enschede, The Netherlands, from 2009 to 2014. He is currently a Chief Executive Officer of the Tyndall National Institute, Cork, Ireland. He has been a Series Editor of the *IET Book Series on Telecommunications and Networking*.

Dr. Scanlon was a recipient of the Young Scientist Award from URSI in 1999 and the 2010 IEEE H. A. Wheeler Prize Paper Award for the IEEE TRANSACTIONS ANTENNAS AND PROPAGATION. He delivered the 2012 NATO International Lecture Series on Next Generation Communications. He was an Inaugural Associate Editor of the IEEE JOURNAL OF TRANSLATIONAL ENGINEERING IN HEALTH AND MEDICINE. He served as an Associate Editor for IEEE ANTENNAS AND WIRELESS PROPAGATION LETTERS. He has served as a Keynote Speaker for the International Symposium on Antennas and Propagation in 2018, the IEEE International Microwave Workshop Series on RF and Wireless Technologies for Biomedical and Healthcare Applications in 2014, the NATO Military Communications and Information Systems Conference in 2010, the International Conference on Bodynets in 2010 and 2018, and the European Workshop on Conformal Antennas in 2007.